



Earth and Space Science



RESEARCH ARTICLE

10.1029/2024EA003589

Reconstruction of Nearshore Surface Gravity Wave Heights From Distributed Acoustic Sensing Data

Samuel Meulé¹ , Julián Pelaez-Quiñones^{2,3}, Frédéric Bouchette⁴, Anthony Sladen², Aurélien Ponte⁵ , Annika Maier⁶, Itzhak Lior⁷, and Paschal Coyle⁸

¹Aix Marseille Univ, CNRS, IRD, INRAE, CEREGE, Aix-en-Provence, France, ²Observatoire de la Côte d'Azur, Géoazur, CNRS, IRD, Université Côte d'Azur, Valbonne, France, ³Now at the Department of Physics and Technology, University of Bergen, Bergen, Norway, ⁴Geosciences-Montpellier, CNRS, University of Montpellier, Montpellier, France, ⁵Laboratoire d'Océanographie Physique et Spatiale, CNRS, IFREMER, IRD, IUEM, Université de Brest, Brest, France, ⁶Karlsruhe Institute of Technology, Karlsruhe, Germany, ⁷Institute of Earth Sciences, The Hebrew University, Jerusalem, Israel, ⁸CNRS/IN2P3, CPPM, Aix-Marseille Univ., Marseille, France

Key Points:

- A simple transfer function between Distributed Acoustic Sensing (DAS) and a collocated pressure sensor is retrieved for surface gravity waves heights
- Ocean waveheights are correctly reconstructed from nearshore DAS measurements
- The signals recorded by DAS can be described from the standpoint of the linear wave theory

Supporting Information:

Supporting Information may be found in the online version of this article.

Correspondence to:

S. Meulé,
meule@cerege.fr

Citation:

Meulé, S., Pelaez-Quiñones, J., Bouchette, F., Sladen, A., Ponte, A., Maier, A., et al. (2024). Reconstruction of nearshore surface gravity wave heights from distributed acoustic sensing data. *Earth and Space Science*, 11, e2024EA003589. <https://doi.org/10.1029/2024EA003589>

Received 17 FEB 2024

Accepted 14 AUG 2024

Author Contributions:

Conceptualization: Samuel Meulé, Julián Pelaez-Quiñones, Frédéric Bouchette, Anthony Sladen, Aurélien Ponte, Annika Maier, Itzhak Lior
Data curation: Samuel Meulé, Julián Pelaez-Quiñones, Frédéric Bouchette
Formal analysis: Samuel Meulé, Julián Pelaez-Quiñones, Frédéric Bouchette, Anthony Sladen
Funding acquisition: Frédéric Bouchette, Anthony Sladen
Methodology: Samuel Meulé, Julián Pelaez-Quiñones, Frédéric Bouchette, Anthony Sladen

Abstract Distributed Acoustic Sensing (DAS) is a photonics technology converting seafloor telecommunications and optical fiber cables into dense arrays of strain sensors, allowing to monitor various oceanic physical processes. Yet, several applications are hindered by the limited knowledge of the transfer function between geophysical variables and DAS measurements. This study investigates the quantitative relationship between surface gravity DAS-recorded wave-generated strain signals along the seafloor and the pressure at a collocated sensor. A remarkable linear correlation is found over various sea conditions allowing us to reliably determine significant wave heights from DAS data. Utilizing linear wave potential theory, we derive an analytical transfer function linking cable deformation and wave kinematic parameters. This transfer function provides a first quantification of the effects related to surface gravity waves and fiber responses. Our results validate DAS's potential for real-time reconstruction of the surface gravity wave spectrum over extended coastal areas. It also enables the estimation of waves hydraulic parameters at depth without the need from offshore deployments.

Plain Language Summary Distributed Acoustic Sensing (DAS) technology converts submarine communication cables into real-time networks of thousands of seismo-acoustic sensors. The high sensitivity of DAS measurements (nano-deformation) makes the recorded signals extremely rich in information, and capable of capturing multiple oceanographic processes. Numerous applications can be envisaged such as monitoring turbidity currents, tsunamis, marine renewable energy parks, etc., and some are already in progress, including monitoring surface vessels, marine currents, cetaceans, etc. However, despite all these developments, the relationship between DAS measurements and certain key ocean variables remains poorly understood. In the littoral zone, this study aims to investigate the link between the deformation signals recorded by DAS due to wave passage at the sea surface and the pressure measured by a sensor located nearby, at the bottom. Our findings demonstrate a strong correlation under varying sea conditions. This correlation allows to reliably determine significant wave heights using DAS data. By applying a simplified theory of wave propagation, the linear wave theory, it was possible to develop an analytical transfer function that relates cable deformation to wave movement parameters. The results confirm that DAS has the potential to reconstruct parameters associated with ocean waves, and could ultimately facilitate their real-time estimation.

1. Introduction

Distributed Acoustic Sensing (DAS) instruments can provide highly sensitive measurements of various environmental physical fields at meter-resolutions along tens to hundreds of kilometers of optical fibers, like those embedded in telecommunication cables (Hartog, 2000; Y. Li et al., 2021; López-Higuera, 2002; Ip et al., 2023). Some of these physical fields include: acoustic wavefields (e.g., Bouffaut et al., 2022; Rivet et al., 2021; Wilcock et al., 2023), seismic wavefields (e.g., T. Dean et al., 2017; Jousset et al., 2022; Tonegawa et al., 2022; H. F. Wang et al., 2018; Zhan, 2019) and temperature anomalies (e.g., Ide et al., 2021; Miller et al., 2018; Pelaez Quiñones et al., 2023).

In underwater environments, the possibility to describe various characteristics of surface gravity waves with DAS has also been exploited in previous works (Guerin et al., 2022; Landrø et al., 2022; Lindsey et al., 2019; Sladen

© 2024. The Author(s).

This is an open access article under the terms of the [Creative Commons Attribution-NonCommercial-NoDerivs License](#), which permits use and distribution in any medium, provided the original work is properly cited, the use is non-commercial and no modifications or adaptations are made.

Resources: Frédéric Bouchette, Anthony Sladen, Paschal Coyle
Validation: Samuel Meulé, Julián Pelaez-Quiñones
Visualization: Samuel Meulé, Julián Pelaez-Quiñones
Writing – original draft: Samuel Meulé, Julián Pelaez-Quiñones, Frédéric Bouchette, Anthony Sladen
Writing – review & editing: Samuel Meulé, Julián Pelaez-Quiñones, Anthony Sladen, Aurélien Ponte, Annika Maier, Itzhak Lior, Paschal Coyle

et al., 2019; Taweessintananon et al., 2023; Williams et al., 2019, 2022; Xiao et al., 2022). In particular, Glover et al. (2023) presented empirical evidence of a correlation existing between seafloor DAS and wave-generated underwater pressure in coastal marine environments. Building upon these previous studies, our study focuses on: (a) reconstructing surface gravity wave heights from DAS measurements in a nearshore environment and (b) developing a theoretical formalism for comparing the energy associated with optical fiber deformation to the energy generated by surface gravity wave action at the sea bottom.

DAS has recently emerged as a promising technology to complement traditional nearshore observational techniques. It offers significant advantages in spatial and temporal resolution for near-bed measurements at a relatively low cost. DAS allows for high-frequency data collection along submarine cables with meter-scale spatial resolution spanning tens to hundreds of kilometers. This capability translates into thousands of sampling locations along the cable route, providing extensive coverage of coastal and nearshore environments. The ability to capture data at kilohertz frequencies enhances the detailed monitoring of wave dynamics, including wave heights and other key parameters, with unprecedented granularity. This comprehensive spatial and temporal coverage makes DAS a powerful tool for advancing our understanding of nearshore processes, improving coastal management practices, and enhancing hazard response capabilities.

Our analysis, encompassing various sea-state conditions, shows that the response of DAS to the kinematics of nearshore surface gravity waves can be well approximated by the linear gravity wave theory. This implies, amongst others, that the nearshore wave spectrum can be inferred at high spatial resolution from DAS data. Additionally, we introduce a relationship to quantify the transfer function between the waves and the fiber.

2. Experimental Setup for the DAS and Pressure Sensor

At the end of 2020, DAS and in situ pressure sea floor observations were collected in the bay of Les Sablettes, Saint-Mandrier-sur-Mer, in the South of France (Figure 1) (Bouchette et al., 2023). A chirped-pulse ϕ -OTDR (phase-sensitive optical time-domain reflectometry) hDAS (High fidelity distributed acoustic sensor) interrogator (Pastor-Graells et al., 2016) providing measurements in strain units was connected to the land termination of the Laboratoire Sous-marin Provence Méditerranée (LSPM) seafloor cable (previously known as the MEUST-NumerEnv cable) (Sladen et al., 2019). This 50 km-long cable extends cross-shore from the coast to the bottom of the NW Mediterranean basin (Figure 1). The acquisition was configured to sample every 10 m along the cable (same spatial sampling and gauge length) at 250 Hz. During the installation, the cable was buried 50 cm to 2 m deep along the first ~500 m from the shoreline. Beyond that, the cable lays on the seafloor, as confirmed by visual surveys over the past 10 years.

Bottom hydraulic pressure data was sampled at 8 Hz between 23 December 2020 to 6 January 2021 with an RBR virtuoso³ pressure sensor deployed at 15 m depth. The initial accuracy of the pressure sensor is ± 1.0 cm with a resolution of 2 mm. The sensor was located about 1 km from the shoreline, next to an exposed cable section. To correct for dynamic pressure, atmospheric pressure measurements were retrieved from the HTMNET station in Saint Elme Harbor, on the eastern edge of the bay (Figure 1). The collocated channel of the DAS with the pressure sensor was identified as channel 260.

Swell propagation can be assumed to be nearly constant in direction and close to aligned with the cable azimuth at the cable section of interest, where the collocated RBR sensor lies. This is a reasonable assumption considering the evenly-sloping bay configuration of Les Sablettes and its shallow water depths (~15 m), meaning that swells are refracted along the cross-shore profile covered by the first few kilometers of cable. The gentle slope of approximately 1.66% further indicates that the beach is not reflective but rather dissipative which is also supported by the f-k diagram (please refer to Figure S1).

3. Experimental Analyses

In the following, we describe the empirical relationship between seafloor DAS and RBR pressure data and validate our ability to reconstruct ocean wave heights from DAS measurements, considering that the RBR pressure signal is known to convey reliable estimates.

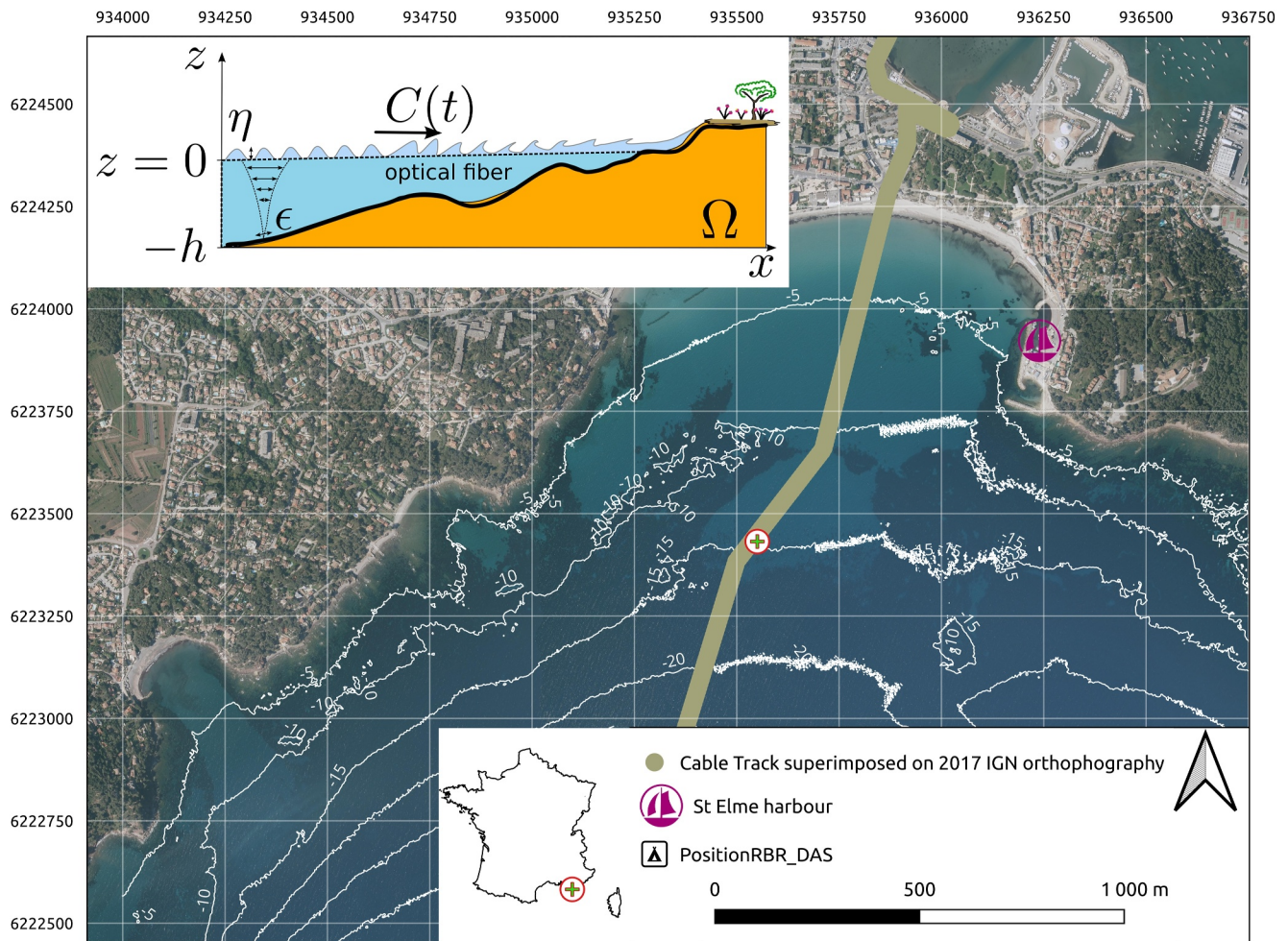


Figure 1. Aerial image of the bay of Les Sablettes (local coordinates). The isobaths in meters were extracted from the LITTO3D® PACA 2015 program. The position of the Laboratoire Sous-marin Provence Méditerranée cable is indicated by the light ocre track and the RBR sensor by the cross and red circle marker. The collocated channel of the Distributed Acoustic Sensing (DAS) with the pressure sensor was identified as channel 260. The top-left inset figure is a schematic description of the experiment as a function of depth with the main physical variables indicated.

3.1. Empirical Relationship Between Seafloor DAS and Pressure Measurements

DAS strain time series in Figures 2a and 2b, are highpassed at 10 mHz (with prior demeaning and tapering) for visualization to remove a non-stationary trend which is known to be fundamentally related to low-frequency temperature effects (e.g., Fang et al., 2012; Ide et al., 2021; Rathod et al., 1994). To match the sampling frequency of the pressure sensor (8 Hz), the DAS data were low-pass filtered (4 Hz) and re-sampled (8 Hz) (Figure 2a).

The signal in Figure 2b represents the raw pressure from the RBR sensor. Pressure-derived kh estimates (k = angular wavenumber, h = water depth) in Figure 2c, indicate that the intermediate-depth wave regime assumption ($\frac{1}{20} < \frac{h}{\lambda} < \frac{1}{2}$, with λ = wavelength) is reasonable over the whole time series. To quantitatively describe the transfer function between DAS strain and sea floor pressure, we focus our analysis on three different weather conditions: fair weather, light gale and moderate storm (Figure 2). These weather conditions are identified from the seafloor pressure data and derived parameters, for example, wave heights H_s and peak frequency f_p as detailed below (see Section 3.2).

Despite some similarities in the time series at the scale of the experiment (Figures 2a and 2b), individual oscillations of the pressure and DAS signals show a clear mismatch in phase as depicted in the 2-min window time series Figure 3. This observed phase mismatch may arise from various factors: (a) imperfect collocation of both

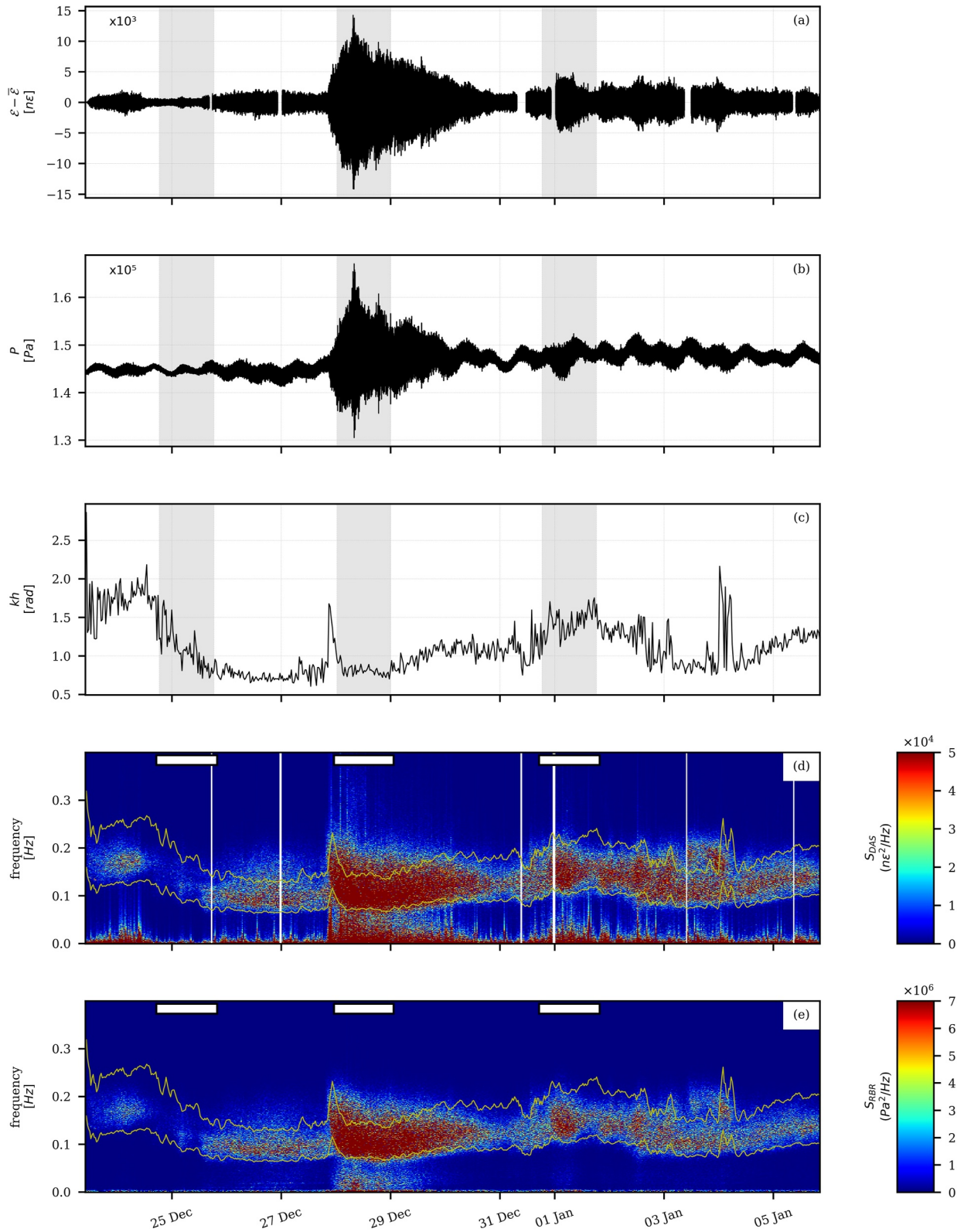


Figure 2.

sensors; (b) differences in measurement nature the pressure sensor provides local absolute measurements whereas DAS data are spatially differentiated measurements which has some consequences on the frequency content of the signals (T. Dean et al., 2017); (c) the physical mechanisms recorded may not solely be linked to ongoing gravity waves. Regarding the latter, surface seismic waves such as Love and Rayleigh waves, generated at shallow depths directly below shallow groundwater regions, can cause strain in the DAS fiber—a well-documented phenomenon in seismology. As waves dissipate energy traveling toward the shore, seismic waves generated near the shore are expected to have lower energy compared to those generated by ocean waves directly. Reflection waves could also explain the observed phase mismatch between DAS and RBR data; however, in the gently sloping bay configuration, reflection from the shore is anticipated to be minimal. For all these reasons, we proceed with a spectral analysis to better understand the frequency content and behavior of the signals despite the observed phase differences.

Spectrograms of seafloor pressure and DAS strain signals (Figures 2d and 2e) were computed over a 15-day period using 30-min non-overlapping windows. Different window durations (10, 20, 30, and 60 min) are tested to observe its influence on the results in Section 3.2. It can be seen that the DAS and RBR spectral density distributions are visually similar within the surface gravity wave band ($f \approx 0.04\text{--}0.3$ Hz, i.e., $T \approx 3\text{--}25$ s). Most of the surface gravity waves energy is clustered between 0.1 and 0.2 Hz. During the high-energy events, DAS records energy in the 0.2~0.4 Hz frequency range which is not clearly captured by the RBR. Infragravity wave content (usually 0.03~0.003 Hz (Bertin et al., 2018), and here $\lesssim 0.04$ Hz) on the RBR is minimal during the observation period, except during the storm on the 28 December, where the DAS signals also shows clear infragravity energy. Infragravity wave activity appears recurrent on DAS for the observation period, but this may partially overlap with temperature-related signals.

Peak frequency time series, $f_p(t_w)$, was derived from pressure spectrograms within the surface gravity wave band ($f \approx 0.04\text{--}0.3$ Hz) for each time window, t_w . Subsequently, more accurate time-varying bounds for the surface gravity wave band were empirically estimated as $[f_p/1.5, f \times 1.5]$. These are superimposed onto spectrograms in Figures 2d and 2e (yellow curves). The spectral energy E was then calculated by integrating the spectral density S within the time-variant wave band for both the RBR pressure sensor and the DAS measurement:

$$E(t_w) = \int_{f_p(t_w)/1.5}^{1.5 \cdot f_p(t_w)} S(f, t_w) df \quad (1)$$

Figure 4 demonstrates a strong linear correlation between E_{DAS} and E_{RBR} . The coefficient of determination (R^2) for a 30-min window is 0.95, attesting to the robustness of the observed relationship. The black patches observed in Figure 4 correspond to variable energy levels, ranging from low to high, in the specific weather conditions of fair-weather, light gale, and moderate storm. Other regressions, such as quadratic regression, were tested but were not optimal, underestimating the lowest energies, and are therefore not shown in Figure 4.

Based on the aforementioned parameters, we obtain the following relationship for the linear regression between DAS and RBR spectral energies:

$$E_{RBR} = \beta E_{DAS} \quad (2)$$

with $\beta = 93.86$

The choice of frequency band for surface gravity waves has a relatively weak effect on the estimated average β value (as long as we remain within the range of gravity waves). For instance, a calculation boundary of $(2f_p, f_p/2)$ results in $\beta = 91.75$ ($R^2 = 0.95$). Fixed boundaries at (0.05, 0.3) Hz provided $\beta = 91.49$ ($R^2 = 0.95$).

Figure 2. Time series of (a) mean-centered and high-passed at 10 mHz (4-pole Butterworth filter) Distributed Acoustic Sensing (DAS) signal, (b) pressure sensor signal (P in Pa), and (c) kh (in rad.) derived from the pressure sensor. The wave number k was calculated from the peak frequency using Equation 7 (see Section 4.1). (d) Spectrogram of the DAS signal with outliers removed (white patches). (e) Spectrogram of the pressure sensor signal. The frequency (f) integration limits ($1.5f_p, f_p/1.5$) are represented by yellow lines. Three selected periods (in chronological order (i) fair-weather condition (ii) storm condition, and (iii) light gale condition), are represented by gray shaded boxes for (a)–(c) and in white patches on top of (d) and (e).

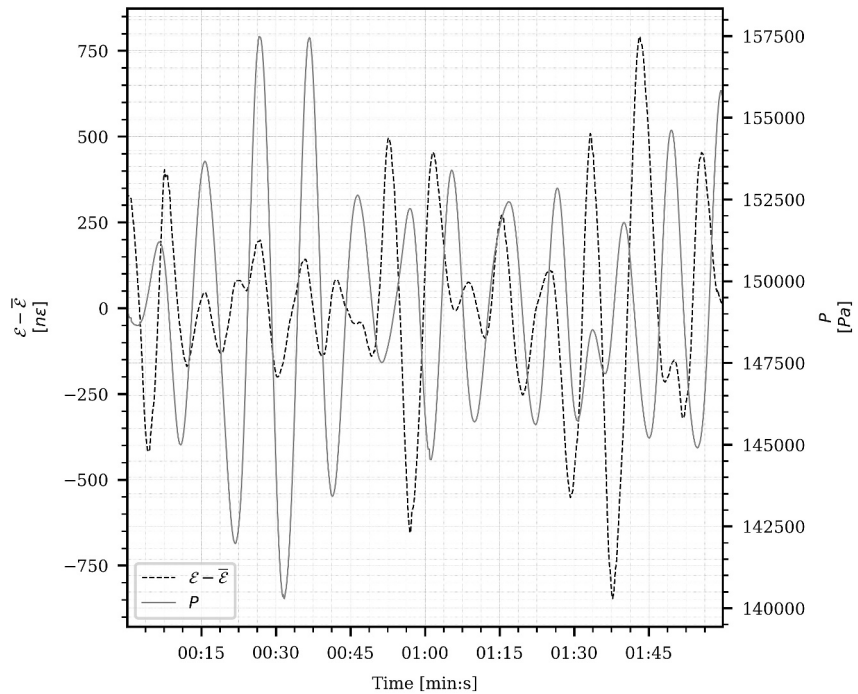


Figure 3. Time series of 2-min window mean-centered and high-passed at 10 mHz (4-pole Butterworth filter) of the 8 Hz Distributed Acoustic Sensing signal in dashed line and time series of 2-min window of the 8 Hz pressure sensor signal (P) in solid line. The data starts at 12:00 28 December 2020.

3.2. Wave Heights Reconstruction From DAS Measurements

Finally, using the β coefficient, it is possible to convert E_{DAS} from nanostrain² to Pa² and subsequently to meters using the hydrostatic pressure equation. To account for the reduction in wave energy or pressure with depth due to the viscosity of the fluid and the natural decay of wave effects, we apply a viscous attenuation correction. This correction compensates for these effects by adjusting E_{DAS} at depth z using the linear theory formula $E(t_w)_c = E(t_w) \frac{\cosh(k(h+z))}{\cosh(kh)}$.

Then, following Horikawa (1988), we calculate the significant wave height, using the relationship $H_s = 4\sqrt{m_0}$, where m_0 represents the zeroth moment of the wave spectrum, which can be directly derived from E_{DAS_c} .

$$H_s(t_w) = 4\sqrt{E(t_w)_c} \quad (3)$$

Figure 5a shows the time series of H_s calculated from the RBR pressure sensors and the DAS signal, while Figure 5b summarizes different performance indicators of such procedure. This illustrates the remarkable accuracy of H_s estimates from DAS. Notably, for a 30-min window, we achieve a coefficient of determination (R^2) of 0.95 and a Mean Absolute Percentage Error of 18.023. However, it is necessary to clarify that this high R^2 value is to be expected due to the initial strong correlation between DAS and RBR spectral energies. Since both energies were converted to wave height using the same Equation 3, assuming linear wave theory, the excellent agreement is primarily a result of this underlying mathematical relationship. While this confirms the consistency of our method, it also emphasizes that the remarkable agreement is essentially due to the prior correlation in spectral energy.

4. Theoretical Framework

So far, we have presented an empirical correlation between DAS and pressure sensor signals. In the following, we develop a formalism to describe this correlation physically, from the standpoint of gravity wave kinematics.

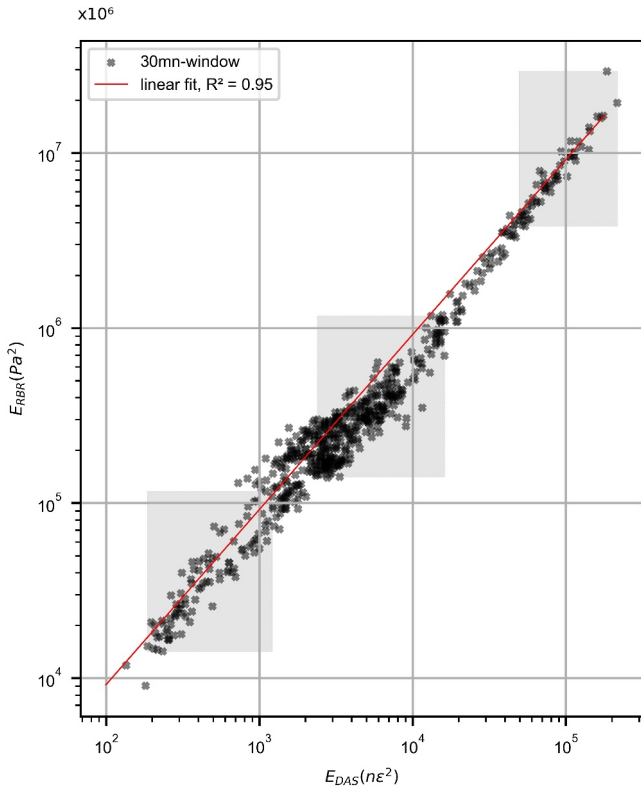


Figure 4. Bivariate correlation plot between the Distributed Acoustic Sensing (DAS) and RBR pressure data. Best-fit linear (with zero y-intercept) is shown in continuous red. The three shaded boxes superimposed on the figure represent (from left-to-right): (i) fair-weather condition (ii) light gale condition and (iii) storm condition.

4.1. Conceptual Model of Cable-Wave Interactions

We start with a system Ω made of a water mass forced by waves coupled to a fiber cable coupled to the seabed as shown in Figure 1, along which the wave-driven action remains spatially homogeneous. In the following, the physical quantities are given in a coordinate framework where the origin is at the still water level, z is positive upward, and x is positive landward (i.e., positive in the direction of wave propagation). In this setting, h is the mean water depth (a positive constant over time scales of the order of hours), $C(t)$ is the wave celerity, $u(x, z, t)$ and $w(x, z, t)$ are the instantaneous horizontal and vertical components of the water velocity, $p(x, z, t)$ is the instantaneous dynamic pressure of the water at depth z , $\tau(x, t)$ is the shear stress at the water-seabed interface driven by waves, $\mathbf{E}(x, t)$ is the ratio of deformation of the fiber cable per unit length along the cable (strain, a dimensionless unit).

To explore the relationship between DAS and pressure sensor signals, we consider the framework of the linear wave potential theory (R. G. Dean & Dalrymple, 1984; Mei, 1992). Following this assumption, we consider a velocity potential Φ on Ω that satisfies

$$\begin{cases} \Delta\Phi = \Phi_{xx} + \Phi_{zz} = 0 & \\ w = \phi_z = 0 & \text{at the sea bottom } z = -h \\ (\Phi_t)_{z=0} = \frac{\partial\eta}{\partial t} & \text{Kinematic surface boundary condition} \\ (\Phi_t + g\eta)_{z=0} = C(t) & \text{Dynamic surface boundary condition} \end{cases} \quad (4)$$

where g is Earth's gravity. The set of Equation 4 forms a well-posed Laplace problem describing the evolution of a water mass forced by waves propagating over a horizontal rigid bottom at which fluid velocity nullifies. One solution for this system is:

$$\Phi(x, z, t) = \frac{ag}{\omega} \frac{\cosh k(h+z)}{\cosh kh} e^{(kx-\omega t)} \quad (5)$$

where a is the amplitude, $\omega = 2\pi/T = 2\pi f$ is the angular frequency (T being the period), and k the wave number of the propagating wave.

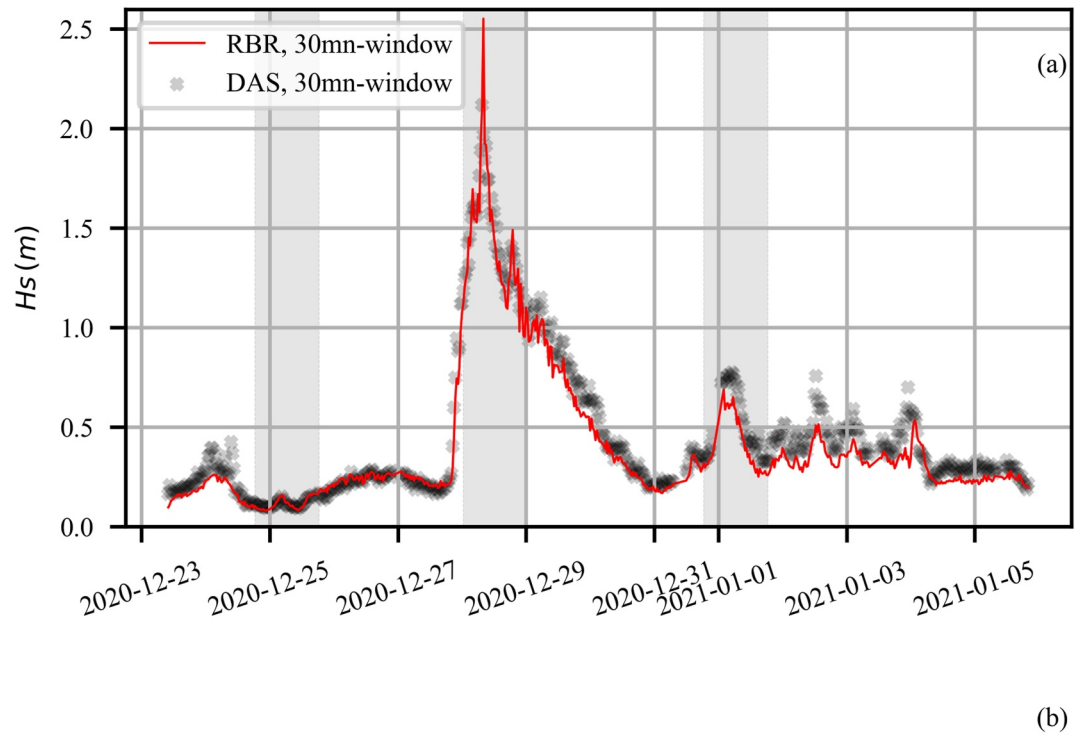
We assume also that wave quantities satisfy the surface gravity wave linear dispersion equation

$$\omega^2 = gk \tanh(kh) \quad (6)$$

which can be approximated following Guo (2002) by:

$$k = \frac{\omega^2}{g} \left(1 - e^{-(\omega^2 h/g)^{5/4}}\right)^{2/5} \quad (7)$$

From the simple theoretical framework formed by Equations 4–7, we could derive most of the hydraulic quantities in Ω , including the dynamic pressure in the presence of waves $p = -\rho(gz - \Phi_t)$, where ρ is the density of water in [$\text{kg} \cdot \text{m}^{-3}$]. However, we do not intend to relate instantaneous hydraulic quantities to the instantaneous deformation of the fiber cable directly. Instead, we relate the fiber cable strain \mathbf{E} to the amplitude of some hydraulic quantities expressed at the sea bottom where the coupling occurs, assuming also that the physics are the same at any point along the abscissa axis in Ω . For designating such a transformation, we use capital letters in relation with the lowercase letter representing the physical quantity concerned (e.g., B for b , where b can be any wave parameter, such as pressure or orbital speed). Then we define the following operator:



Window size (mn)	RMSE	MAE	R ²	Error rate
10	0.008	0.063	0.94	18.308
20	0.007	0.06	0.949	17.816
30	0.006	0.06	0.95	18.023
60	0.007	0.061	0.947	18.917

Figure 5. (a) Estimated wave height time series for Distributed Acoustic Sensing (DAS) and RBR. Three selected shaded boxes were superimposed on the figure, representing (i) fair-weather condition (ii) storm condition and (iii) light gale condition. In Table (b), error statistics are summarized as a function of window size (in mins). RMSE, root mean square error; MAE, mean absolute error; R^2 , coefficient of determination; Error Rate, mean absolute percentage error.

$$B = \frac{1}{2} \left(\left| \max [b(x, z, t)|_{z=-h}]_{t \in \delta T} \right| + \left| \min [b(x, z, t)|_{z=-h}]_{t \in \delta T} \right| \right) \quad (8)$$

where δT is a time interval representative of some wave periods. The quantity B is homogeneous along the abscissa axis so that x can be removed from the formula.

Following this naming convention, we calculate three quantities: (a) P^+ , the amplitude of the excess of pressure at the sea bottom due to waves defined after the amplitude of the total pressure $P = \rho gh + P^+$; (b) U_{orb} the amplitude

of the horizontal component of orbital velocity oscillations at the sea bottom; (c) X_{exc} the horizontal excursion of water particles at the sea bottom:

$$P^+ = \frac{\rho a g}{\cosh(kh)} \quad (9)$$

$$X_{exc} = \frac{a}{\sinh(kh)} \quad (10)$$

The three equations above relate the properties of surface gravity waves to hydraulic quantities at the sea bottom, but they cannot be directly related to the DAS measurements without also expressing the kinematic and dynamic conditions between the water at the sea bottom and the sediment and fiber-optic cable.

4.2. Definition of the Water—Cable Coupling

We examine the simple case where the horizontal motion of the water would drive the axial/longitudinal deformation of the fiber cable by simple shearing. If the fiber cable was perfectly coupled with the water (possibly through the seabed), X_{exc} would represent the amplitude of the longitudinal displacement of the fiber cable during a wavelength. The deformation of the fiber would be defined by the ratio $X_{exc}k/2\pi$ for a gauge length (10 m), which is smaller than the wavelength. Obviously, in such a case, the fiber deformation would be by far beyond its elastic behavior; in practice, only a small amount of the water deformation—let us say a ratio α —may be transmitted to the fiber cable. \mathbf{E} could then be written after this ratio α and X_{exc} :

$$\mathbf{E} = \frac{\alpha k a}{2\pi \sinh(kh)} \quad (11)$$

5. Deriving a More Physically-Informed Expression of the Coefficient β

Using field measurements, we have shown that there is a linear relationship by an empirical factor β (from Equation 2, here renamed β_e), between the power spectral density of the deformation of the fiber E_{DAS} (in nanostrain²) and that of the pressure (in Pa²) induced at the ocean bottom by the propagating waves. The previously derived equations allow us to derive a similar expression based on linear wave theory since P^+ on the sea bottom is linked to surface gravity waves via Equation 9, and to the DAS measurement via Equation 11

$$(P^+)^2 = \beta_e \mathbf{E}^2 \quad (12)$$

Combining Equations 11 and 12, we obtain:

$$\mathbf{E} = \alpha \frac{P^+ k}{2\pi \rho g \tanh(kh)} \quad (13)$$

Based on Equation 13, we can evaluate α . For the peak storm (the 28 December at 8:00, see Figure 2), the peak period is $T_p = 10.6$ s. We take the cable depth $h = 14.6$ m in a water of mean density $\rho = 1,028$ kg/m³. From Equation 9, the estimated excess of pressure for a wave of amplitude $a = H_s/2 \approx 1.2$ m (from Figure 5) is $P^+ \approx 9.1$ kPa. From all these values, we can anticipate that the parameter α would be on the order of 1.2×10^{-4} .

Squaring Equation 13, we can extract a modeled β factor (β_m)

$$\beta_m = \frac{1}{\alpha^2} \frac{4\pi^2 \rho^2 g^2 \tanh^2(kh)}{k^2} \quad (14)$$

Using the dispersion relation (Equation 6), we obtain a new relationship for β_m :

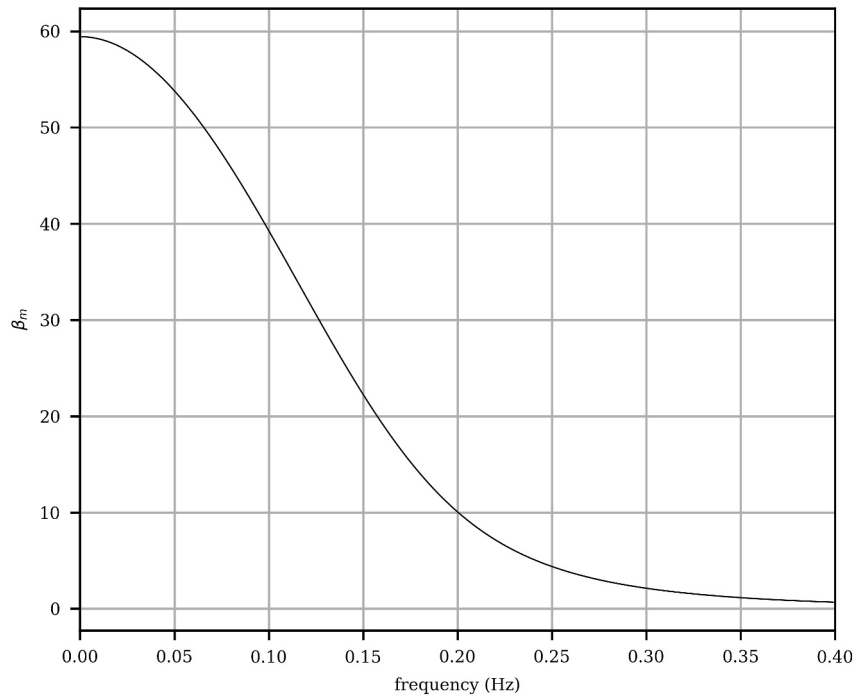


Figure 6. β_m as a function of frequency from Equation 15, using $h = 14.6$ m, $\rho = 1,028$ kg/m³ and assuming a constant α value of 1.2×10^{-5} (estimated following Equation 13 as in the Discussion section, with Distributed Acoustic Sensing in nanostrain units).

$$\beta_m = \frac{1}{\alpha^2 \gamma^2} \quad (15)$$

$$\text{with } \gamma = \frac{1}{2\pi\rho C^2}$$

We can compare the empirical β_e coefficient estimated from windowed linear regressions of the spectral energy of strain and pressure with a modeled β_m derived from Equation 15. α is retrieved from Equation 13 by taking P^+ and \mathbf{E} from the data, while γ is derived from $C = 2\pi(kT_p)^{-1}$, where k is estimated from T_p via Equation 7. The relationship between the empirical and modeled β is illustrated in Figures 7a and 7b for 5 and 30 mn-window analysis. Although the linear relationship captures only a limited fraction of the variability in the data ($R^2 = 0.58$ for 5 m-window and $R^2 = 0.53$ for 30 m-window), most points are clustered around the identical function, demonstrating a substantial degree of agreement between the two β values. This supports the applicability of the linear theory to describe the energy transfer mechanism from surface gravity waves into the cable. From Equation 15, it is suggested that β is frequency-dependent, which may explain its window-wise variability. This is confirmed by the clustered distribution of the peak period in Figure 7b, which shows that β values are proportional to wave period, in agreement with Equation 15. As a confirmation of this relationship, Figure 6 illustrates β as a function of wave frequency for a given set of parameters.

Time series of the distribution of empirical and modeled β values over time for 30-min spectral energy windowing confirms the agreement between both estimates (Figure 7c).

From Equation 15, it appears that the transfer coefficient between the wave pressure signal and the DAS strain signal β is characterized by two parameters: γ , which can be considered the fluid- or wave-related factor. This term represents the kinematics of the water oscillations that cause the cable deformation; and α , which represents both, the fraction of wave displacements that is effectively transmitted into the fiber and the dynamic response of the fiber, that is, a superposition of physical conditions related to the structural and material characteristics of the cable, its coupling nature to the seabed, and the specific visco-elastic mechanism(s) of stress transfer from the fluid into the cable. At this stage, it remains challenging to separate these different effects, but we stress that the α

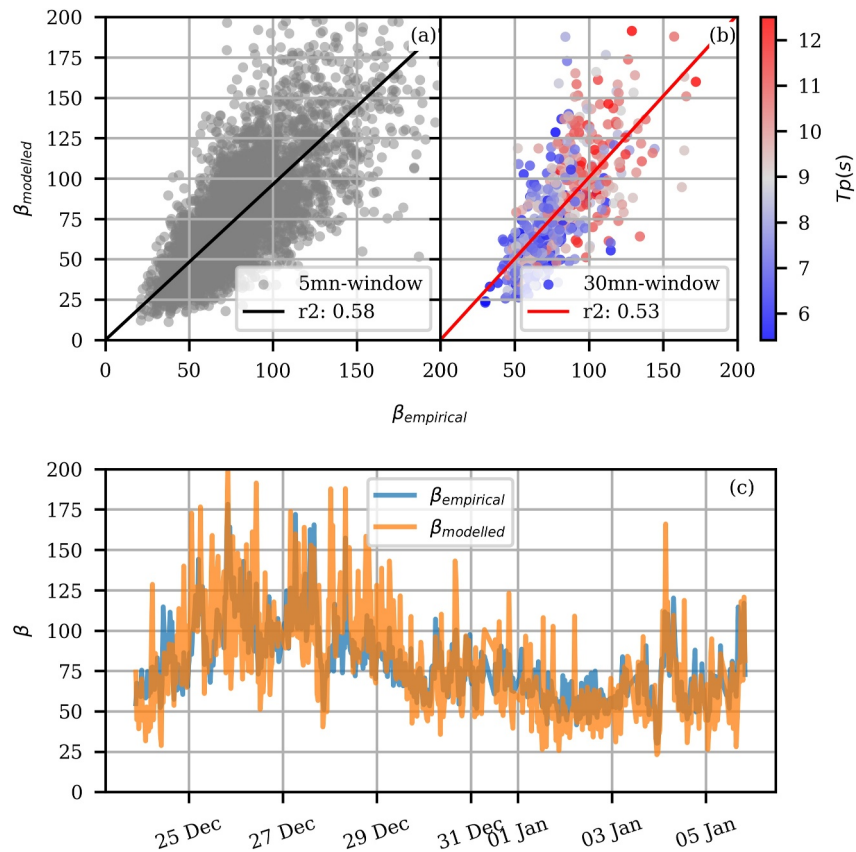


Figure 7. Bivariate correlation plot between empirical and modeled β (a) for 5-min spectral energy estimates and (b) for 30-min estimates as a function of the peak period (T_p (s)). Best-fit linear (with zero y-intercept) is shown in continuous red. Note that the best linear fit nearly matches the identical function ($x = y$). The lower panel (c) depicts the temporal distribution of the scatter in (b).

parameter is subject to further parameterization and decomposition based on more advanced dynamic and elasto-mechanical considerations, as well as more detailed observations.

6. Discussion

We have established a correlation between cable deformation and wave-induced pressure that can be sufficiently described kinematically. However, such correlation with pressure is not necessarily causal, as the specific mechanisms transferring stresses from the water into the fiber are not fully constrained. Pressure-induced Poisson effect on the cable and/or seabed bending/compliance are both often considered to participate in fiber deformation. For instance, previous studies have attributed the observation of surface gravity waves to direct dynamic pressure loading (e.g., Glover et al., 2023; Taweestananon et al., 2023). However, the linear wave theory predicts similar depth-dependent functions and oscillation patterns for both, the wave-induced dynamic pressure and the horizontal component of the orbital acceleration motions. The latter could exert important shear stresses via boundary layer-seabed friction and/or via differential shearing of the cable structure, which could in turn cause axial fiber elongation. The second mechanism may be less significant, considering the high shear modulus of silica ($\sim 10^9$ Pa) (López-Higuera, 2002). However, the shear modulus of silicon coatings can be as low as $\sim 10^6$ Pa (D. Li et al., 2012; H. Wang et al., 2018), while dynamic wave pressure values at the seafloor are generally much larger than its corresponding shear stresses. For instance, the estimated maximum excess pressure during the peak storm as previously estimated from Equation 13 is ~ 9.1 kPa, while the maximum shear stress $\tau = \frac{1}{2}\rho f_w U_{orb}^2$ for a typical seabed friction coefficient f_w of 0.1 (Hardisty, 1990; You & Yin, 2007) is estimated around 33 Pa for the same wave (330 Pa for a relatively high $f_w = 1$). On the other hand, considering the predominantly axial strain sensitivity of optical fibers (Kuvshinov, 2016; Papp et al., 2017), it may still occur that the deformations

effectively transferred near-axial shear stresses on the fiber are as relevant or perhaps even more so than those induced by (mostly broadside) dynamic pressure loading. In the case of a sloping seabed, axial dynamic pressure gradients could also develop that potentially induce cable deformations in the form of shear stresses. Additionally, the asymmetry of more realistic, non-sinusoidal nearshore gravity waves is expected to increase seabed shear stresses (Gonzalez-Rodriguez & Madsen, 2007). Further analyses are required to reliably quantify and assess the pressure loading, seafloor compliance and frictional contributions to fiber deformation.

At least, what appears to be relatively well-established is that surface seismic waves, such as Love and Rayleigh waves, have a minor to negligible contribution to the DAS signal, in the surface gravity wave frequency range. As these surface seismic waves travel toward the shore, energy dissipation should occur which is the opposite of what is observed. Previous DAS studies (e.g., Guerin et al. (2022) and Sladen et al. (2019) on our study site, and Williams et al. (2022) across the Strait of Gibraltar) already demonstrated that the origin of the DAS strain signal is due to the direct physical transfer mechanism of ocean gravity waves above the fiber. Our data contains similar signatures, as depicted in the f - k diagram (Figure S1). The observed dispersion characteristics fit well with the theoretical linear dispersion relationship of surface gravity waves (and hence their typical phase speeds). The directional asymmetry of the recorded waves also excludes the possibility that they are seismic surface waves that are expected to also radiate offshore. We also recall that the slope of the beach at Les Sablettes near Toulon has a slope of approximately 1.6%. This gentle slope indicates that the beach is not reflective but rather dissipative. Reflective beaches typically have much steeper slopes (often $>5\%$). Therefore, it is unlikely that wave reflection from the shore is a significant factor in generating the DAS signals. However, seismic waves may have a larger contribution in the case of reflective beaches or systems with coastal cliffs.

Although the coupling of optical fibers to different host structures (e.g., cables with coating, armoring) and that of cables to seabeds with variable materials and fabrics (e.g., sediments, rocks, seagrass) is implicit in the α parameter, the specific ranges of validity and the stability of our transfer function under extreme conditions remain unexplored. For instance, a considerable cable burial degree is expected to attenuate the gravity wave forces, while extreme variations in wave amplitude or direction may influence the transfer function non-linearly. However, no clear saturation effects were observed in the DAS signal during the most energetic storm event, even at high frequencies. This suggests that the high non-linearity of surface waves in a nearshore environment does not compromise the reliability of DAS measurements nor the transfer function. However, it should be noted that this has yet to be confirmed for much harsher wave conditions, such as those present during a hurricane.

Furthermore, the dependence on a collocated pressure sensor for reconstructing the surface gravity wave spectrum is an important consideration. Currently, some key parameters are estimated based on the data from a collocated pressure sensor. Understanding the extent to which the transfer function can be accurately determined without a collocated pressure sensor is a key objective of our ongoing research. To address this, we have deployed multiple immersed stations at varying distances from the DAS array. This setup will help us evaluate the impact of the distance between the pressure sensor and the DAS on the calculation of the transfer function. Our goal is to determine the feasibility of using DAS independently and to quantify any lateral variation in the transfer function along the DAS array. This will enhance our understanding of the robustness and applicability of DAS in different configurations and environments.

7. Conclusion

In this study, we have presented a methodology to construct a simple transfer function between nearshore surface gravity waves and the induced DAS strain on a seafloor fiber optic cable in the frequency band ~ 0.04 – 0.3 Hz and under diverse sea-state conditions. The linear potential wave theory is sufficient to describe the main characteristics of the transfer function from a kinematic standpoint, including its frequency dependence. Our theoretical development also highlights the possibility to quantify the relative contribution of waves and of the cable in this transfer function. The latter currently remains an empirical parameter that could be further decomposed based on more advanced, for example, dynamical, considerations. This reaffirms the major potential of seafloor DAS as a tool for the reconstruction of the nearshore gravity wave spectrum along seafloor cables with spatial resolutions of a few meters.

Additional experimental steps are required to verify the potential dependency of such transfer function (more specifically the α parameter) on cable environment (depth, burial, cable type/integrity) as well as its robustness under an even wider range of swell environments (kh , H_s). The sensitivity, high resolution, and wide coverage of

DAS technology opens up a vast field of ocean research and practical applications, which in addition to the retrieval of significant wave heights as shown in this study, suggests the possibility of extracting and quantifying more complex wave propagation characteristics.

Acronyms

DAS Distributed Acoustic Sensing

Data Availability Statement

The DAS data set was recorded on the seafloor Laboratoire Sous-marin Provence Méditerranée (LSPM) cable south of Toulon, which was part of the Mediterranean Eurocentre for Underwater Sciences and Technologies (MEUST) infrastructure at the time of acquisition (see Sladen et al. (2019) for details) using an Aragón Photonics hDAS interrogator. MEUST is financed with the support of the CNRS/IN2P3, the Region Sud, France (CPER) the State (DRRT), and FEDER.

The data sets for Distributed Acoustic Sensing (DAS) and pressure sensor data used in the reconstruction of nearshore surface gravity wave spectrum from DAS time series are accessible at Bouchette et al. (2023).

Atmospheric pressure measurements used in this study were obtained from the HTMNET station located in the port of Saint Elme. HTMNET, operated by the Mediterranean Institute of Oceanography (MIO), provides real-time environmental data, including atmospheric pressure measurements. The data are available at <https://htmnet.mio.osupytheas.fr/>.

Data processing and analyses largely relied on Python libraries: SciPy (<https://scipy.org/>), NumPy (<https://numpy.org/>), Pandas (<https://pandas.pydata.org/>), Matplotlib (<https://matplotlib.org/>), Dask (<https://www.dask.org/>) and h5Py (<https://www.h5py.org/>).

Acknowledgments

We would like to thank the reviewers for their insightful and constructive comments throughout the revision process of this manuscript. Their suggestions have significantly improved the clarity and quality of our work. We are grateful to GLADYS (<https://www.gladys-littoral.org/>) for the water pressure sensors deployed at the field site Les Sablettes and for all the logistics and funding for the deployment (boat, scuba diving equipment, ...). The HTMNET program (<https://htmnet.mio.osupytheas.fr/>) provided us with the atmospheric data. This project has received financial support from the CNRS through the MITI interdisciplinary programs through its exploratory research program. J.P.Q. was supported by the SEAFOD project, funded by Grant ANR-17-CE04-0007 of the French Agence Nationale de la Recherche, Université Côte d'Azur IDEX program UCA^{JEDI} ANR-15-IDEX-0001, and the Doebelin Federation (FR2800 CNRS), and the project MARMOR, funded by ANR-21-ESRE-0020 of the France 2030 program of the French Agence Nationale de la Recherche.

References

- Bertin, X., de Bakker, A., van Dongeren, A., Coco, G., André, G., Arduin, F., et al. (2018). Infragravity waves: From driving mechanisms to impacts. *Earth-Science Reviews*, 177, 774–799. <https://doi.org/10.1016/j.earscirev.2018.01.002>
- Bouchette, F., Sladen, A., Meulé, S., & Pelaez-Quinones, J. (2023). Das and pressure sensor datasets for the reconstruction of nearshore surface gravity wave spectrum from distributed acoustic sensing time series [Dataset]. *OSU OREME*. <https://doi.org/10.15148/7d5e2f17-bad6-4ac3-87e2-84888d0d6699>
- Bouffaut, L., Taweestitananon, K., Kriesell, H. J., Rørstadbotnen, R. A., Potter, J. R., Landrø, M., et al. (2022). Eavesdropping at the speed of light: Distributed acoustic sensing of Baleen Whales in the Arctic. *Frontiers in Marine Science*, 9, 901348. <https://doi.org/10.3389/fmars.2022.901348>
- Dean, R. G., & Dalrymple, R. (1984). *Water wave mechanics for engineers and scientists*. Prentice Hall.
- Dean, T., Cuny, T., & Hartog, A. H. (2017). The effect of gauge length on axially incident p-waves measured using fibre optic distributed vibration sensing. *Geophysical Prospecting*, 65(1), 184–193. <https://doi.org/10.1111/1365-2478.12419>
- Fang, Z., Chin, K. K., Cai, H., & Qu, R. (2012). *Fundamentals of optical fiber sensors* (pp. 96–97). John Wiley & Sons, Ltd. <https://doi.org/10.1002/9781118381717.ch3>
- Glover, H., Wengrove, M. E., & Holman, R. (2023). Distributed acoustic sensing of nearshore processes in Duck, NC, USA. In *Coastal sediments 2023* (pp. 1576–1583). https://doi.org/10.1142/9789811275135_0146
- Gonzalez-Rodriguez, D., & Madsen, O. S. (2007). Seabed shear stress and bedload transport due to asymmetric and skewed waves. *Coastal Engineering*, 54(12), 914–929. <https://doi.org/10.1016/j.coastaleng.2007.06.004>
- Guerin, G., Rivet, D., van den Ende, M., Stutzmann, E., Sladen, A., & Ampuero, J. P. (2022). Quantifying microseismic noise generation from coastal reflection of gravity waves recorded by seafloor DAS. *Geophysical Journal International*, 231(1), 394–407. <https://doi.org/10.1093/gji/ggac200>
- Guo, J. (2002). Simple and explicit solution of wave dispersion equation. *Coastal Engineering*, 45(2), 71–74. [https://doi.org/10.1016/s0378-3839\(02\)00039-x](https://doi.org/10.1016/s0378-3839(02)00039-x)
- Hardisty, J. (1990). *Beaches: Form and processes*. Unwin Hyman.
- Hartog, A. (2000). Distributed fiber-optic sensors: Principles and applications. In *Optical fiber sensor technology* (pp. 241–301). Springer. https://doi.org/10.1007/978-1-4757-6079-8_4
- Horikawa, K. (1988). *Nearshore dynamics and coastal processes: Theory, measurement, and predictive models* (p. 522). University of Tokyo Press.
- Ide, S., Araki, E., & Matsumoto, H. (2021). Very broadband strain-rate measurements along a submarine fiber-optic cable off Cape Muroto, Nankai subduction zone, Japan. *Earth Planets and Space*, 73(63), 63. <https://doi.org/10.1186/s40623-021-01385-5>
- Ip, E., Huang, Y.-K., Huang, M.-F., Yaman, F., Wellbrock, G., Xia, T., et al. (2023). DAS over 1.007-km hybrid link with 10-Tb/s DP-16QAM Co-propagation using frequency-diverse chirped pulses. *Journal of Lightwave Technology*, 41(4), 1077–1086. <https://doi.org/10.1109/JLT.2022.3219369>
- Jousset, P., Currenti, G., Schwarz, B., Chalari, A., Tilmann, F., Reinsch, T., et al. (2022). Fibre optic distributed acoustic sensing of volcanic events. *Nature Communications*, 13(1), 1753. <https://doi.org/10.1038/s41467-022-29184-w>

- Kuvshinov, B. (2016). Interaction of helically wound fibre-optic cables with plane seismic waves. *Geophysical Prospecting*, *64*(3), 671–688. <https://doi.org/10.1111/1365-2478.12303>
- Landrø, M., Bouffaut, L., Kriesell, H. J., Potter, J. R., Rørstadbotnen, R. A., Taweentananon, K., et al. (2022). Sensing whales, storms, ships and earthquakes using an Arctic fibre optic cable. *Scientific Reports*, *12*, 19226. <https://doi.org/10.1038/s41598-022-23606-x>
- Li, D., Ren, L., & Li, H. (2012). Mechanical property and strain transferring mechanism in optical fiber sensors. In M. Yasin, S. W. Harun, & H. Arof (Eds.), *Fiber optic sensors*. Rijeka: IntechOpen. (Chap. 18). <https://doi.org/10.5772/27731>
- Li, Y., Karrenbach, M., & Ajo-Franklin, J. (2021). A literature review: Distributed acoustic sensing (DAS) geophysical applications over the past 20 years. In *Distributed acoustic sensing in geophysics: Methods and applications* (pp. 229–291). <https://doi.org/10.1002/9781119521808.ch17>
- Lindsey, N. J., Dawe, T. C., & Ajo-Franklin, J. B. (2019). Illuminating seafloor faults and ocean dynamics with dark fiber distributed acoustic sensing. *Science*, *366*(6469), 1103–1107. <https://doi.org/10.1126/science.aay5881>
- López-Higuera, J. M. (Ed.). (2002). *Handbook of optical fibre sensing technology* (1st ed.). John Wiley & Sons, Ltd.
- Mei, C. C. (1992). The applied dynamics of ocean surface waves. In *Advanced series on ocean engineering: Volume 1*. World Scientific. <https://doi.org/10.1142/0752>
- Miller, D. E., Coleman, T., Zeng, X., Patterson, J. R., Reinisch, E. C., Cardiff, M. A., et al. (2018). DAS and DTS at Brady Hot Springs: Observations about coupling and coupled interpretations. In *Proceedings of the 43rd workshop on geothermal reservoir engineering, Stanford, CA, USA* (pp. 12–14).
- Papp, B., Donno, D., Martin, J. E., & Hartog, A. H. (2017). A study of the geophysical response of distributed fibre optic acoustic sensors through laboratory-scale experiments. *Geophysical Prospecting*, *65*(5), 1186–1204. <https://doi.org/10.1111/1365-2478.12471>
- Pastor-Graells, J., Martins, H., Garcia-Ruiz, A., Martin-Lopez, S., & Gonzalez-Herraez, M. (2016). Single-shot distributed temperature and strain tracking using direct detection phase-sensitive OTDR with chirped pulses. *Optics Express*, *24*(12), 13121–13133. <https://doi.org/10.1364/OE.24.013121>
- Pelaez Quiñones, J., Sladen, A., Ponte, A., Lior, I., Ampuero, J.-P., Rivet, D., et al. (2023). High resolution seafloor thermometry for internal wave and upwelling monitoring using distributed acoustic sensing. *Scientific Reports*, *13*(1), 17459. <https://doi.org/10.1038/s41598-023-44635-0>
- Rathod, R., Pechstedt, R. D., Jackson, D. A., & Webb, D. J. (1994). Distributed temperature-change sensor based on Rayleigh backscattering in an optical fiber. *Optics Letters*, *19*(8), 593–595. <https://doi.org/10.1364/ol.19.000593>
- Rivet, D., de Cacqueray, B., Sladen, A., Roques, A., & Calbris, G. (2021). Preliminary assessment of ship detection and trajectory evaluation using distributed acoustic sensing on an optical fiber telecom cable. *Journal of the Acoustical Society of America*, *149*(4), 2615–2627. <https://doi.org/10.1121/10.0004129>
- Sladen, A., Rivet, D., Ampuero, J. P., Barros, L., Hello, Y., Calbris, G., & Lamare, P. (2019). Distributed sensing of earthquakes and ocean-solid Earth interactions on seafloor telecom cables. *Nature Communications*, *10*(1), 5777. <https://doi.org/10.1038/s41467-019-13793-z>
- Taweentananon, K., Landrø, M., Potter, J. R., Johansen, S. E., Rørstadbotnen, R. A., Bouffaut, L., et al. (2023). Distributed acoustic sensing of ocean-bottom seismo-acoustics and distant storms: A case study from Svalbard, Norway. *Geophysics*, *88*(3), B135–B150. <https://doi.org/10.1190/geo2022-0435.1>
- Tonegawa, T., Araki, E., Matsumoto, H., Kimura, T., Obana, K., Fujie, G., et al. (2022). Extraction of P wave from ambient seafloor noise observed by distributed acoustic sensing. *Geophysical Research Letters*, *49*(4), e2022GL098162. <https://doi.org/10.1029/2022GL098162>
- Wang, H., Jiang, L., & Xiang, P. (2018). Improving the durability of the optical fiber sensor based on strain transfer analysis. *Optical Fiber Technology*, *42*, 97–104. <https://doi.org/10.1016/j.yofte.2018.02.004>
- Wang, H. F., Zeng, X., Miller, D. E., Fratta, D., Feigl, K. L., Thurber, C. H., & Mellors, R. J. (2018). Ground motion response to an ML 4.3 earthquake using co-located distributed acoustic sensing and seismometer arrays. *Geophysical Journal International*, *213*(3), 2020–2036. <https://doi.org/10.1093/gji/gyy102>
- Wilcock, W. S. D., Abadi, S., & Lipovsky, B. P. (2023). Distributed acoustic sensing recordings of low-frequency whale calls and ship noise offshore Central Oregon. *JASA Express Letters*, *3*(2), 026002. <https://doi.org/10.1121/10.0017104>
- Williams, E. F., Fernández-Ruiz, M. R., Magalhaes, R., Vanthillo, R., Zhan, Z., González-Herráez, M., & Martins, H. (2019). Distributed sensing of microseisms and teleseisms with submarine dark fibers. *Nature Communications*, *10*(1), 5778. <https://doi.org/10.1038/s41467-019-13262-7>
- Williams, E. F., Zhan, Z., Martins, H. F., Fernández-Ruiz, M. R., Martín-López, S., González-Herráez, M., & Callies, J. (2022). Surface gravity wave interferometry and ocean current monitoring with ocean-bottom DAS. *Journal of Geophysical Research: Oceans*, *127*(5), e2021JC018375. <https://doi.org/10.1029/2021JC018375>
- Xiao, H., Tanimoto, T., Spica, Z. J., Gaité, B., Ruiz-Barajas, S., Pan, M., & Viens, L. (2022). Locating the precise sources of high-frequency microseisms using distributed acoustic sensing. *Geophysical Research Letters*, *49*(17), e2022GL099292. <https://doi.org/10.1029/2022GL099292>
- You, Z.-J., & Yin, B. (2007). Direct measurement of bottom shear stress under water waves. *Journal of Coastal Research*, (SI 50), 1132–1136. (Proceedings of the 9th International Coastal Symposium). <https://doi.org/10.2112/jcr-si50-205.1>
- Zhan, Z. (2019). Distributed acoustic sensing turns fiber-optic cables into sensitive seismic antennas. *Seismological Research Letters*, *91*(1), 1–15. <https://doi.org/10.1785/0220190112>